atmosphere

MDPI

Article

Studying the Impact of LULC Correspondence Between Landsat 8 and Spot 7 Data on Land Surface Temperature Estimation

Yehia Miky

Department of Geomatics, Faculty of Architecture and Planning, King Abdulaziz University, Jeddah 21589, Saudi Arabia; yhhassan@kau.edu.sa; Tel.: +966-541463903

Abstract: Information about land surface temperature (LST) plays a crucial role in environmental studies, as it provides essential data for understanding climate patterns, assessing ecosystem health, and predicting environmental changes. Understanding the relationship between land cover types and LST is crucial across all disciplines that deal with LST data. It helps researchers identify trends in global warming, heatwaves, and cooling effects, which can influence biodiversity, agriculture, and water resources. The accuracy of LST calculations heavily depends on the quality of the data used. However, most satellite thermal data used for LST estimations are in coarse spatial resolution. This study aims to explore the complex interaction between land cover types, considering factors such as proportion and neighboring effects, and LST recalculation by integrating the estimated LST from Landsat thermal band and Spot imagery classification. A machine learning model was employed to quantify the contribution of each Spot pixel to the LST estimated from TIRS data, classifying it as either heating or cooling. The Al Morjan and Al Hamra districts in Jeddah, Saudi Arabia, were used as case studies. The results showed that Spot images achieved a classification accuracy of over 95%, whereas Landsat images did not exceed 77%. The average heating and cooling factors from neighboring pixels were 1.06 and 0.96, respectively. The study demonstrates the improved spatial distribution of LST, with overall temperature increases across all land cover classes. The findings of this study could aid in identifying environmental imbalances and developing effective solutions.

Keywords: LST; landsat; spot; cooling and heating coefficients; LULC; Jeddah

check for updates

Citation: Miky, Y. Studying the Impact of LULC Correspondence Between Landsat 8 and Spot 7 Data on Land Surface Temperature Estimation. *Atmosphere* **2024**, *15*, 1427. https://doi.org/10.3390/atmos15121427

Academic Editor: Thomas Gill

Received: 18 October 2024
Revised: 14 November 2024
Accepted: 26 November 2024
Published: 27 November 2024

Copyright: © 2024 by the author. Licensee MDPI, Basel, Switzerland. This article is an open access article distributed under the terms and conditions of the Creative Commons Attribution (CC BY) license (https://creativecommons.org/licenses/by/4.0/).

1. Introduction

Land surface temperature (LST) is an important variable in the climate system of the Earth [1,2]. LST plays a crucial role in the Earth's surface's energy balance, influencing local and global climates by controlling energy and water exchange between the surface and the atmosphere. It is the main indicator in many applications, such as energy balance studies [3–7], identifying urban heat island (UHI) effects [8–15], climate change studies [16–21], and surface soil moisture and evapotranspiration estimations [22–26]. The most accurate way to determine LST is using field observations. However, it is too difficult to cover a large area with discrete stations. Because of this, the only way to determine LST is through satellite observations, which provide global data at an average pixel scale [2].

Since the 1960s, numerous infrared thermal sensors (TIR) have been installed on different satellites to observe LST, including the Landsat satellite series, the Advanced Spaceborne Thermal Emission and Reflection Radiometer (ASTER), the Moderate Resolution Imaging Spectroradiometer (MODIS), the Earth Observing System Terra and Aqua satellites, and the Advanced Very High-Resolution Radiometer (AVHRR). In the literature, various methods and algorithms have been utilized for retrieving different LST products from TIR data [27–40]. These can be categorized into four methods: the single-channel (SC) method, the split-window (SW) method, the temperature and emissivity separation (TES) method, and the physics-based day/night (D/N) method. No special assumption is

needed for the SC algorithm, but the land surface emissivity (LSE) values must be known. This method is simple and can be applied to all TIR sensors. However, the accuracy of the results depends on the atmospheric profiles [36,41,42]. Unlike the SC algorithm, the SW method does not require atmospheric profiles, however, the LSE of objects is needed. Under high humidity, the accuracy of that algorithm is reduced [29,33,43]. For the TES algorithm, an assumption of the relationship between the range of LSE and the minimum value of LSE is made. In addition, at least three TIR channels are required, and accurate atmospheric correction is needed. The accuracy of this algorithm is highly dependent on the trustworthiness of the empirical relationship [44,45]. For the D/N algorithm, at least one Middle Infrared (MIR) and one TIR channel in atmospheric windows for day and night are required, but accurate atmospheric profiles are not required. Regardless of the similarity of observation angles, LST extraction is not an easy task and requires approximate shapes of atmospheric profiles [31,46].

Indeed, satellite sensors measure radiance influenced by not only the surface parameters such as landcover types, LSE and LST, but also the atmospheric conditions. Therefore, retrieving LST from space is a challenging task that requires more constraints and assumptions to decrease the number of unknowns or increase the number of equations and determine the LST. According to Li Z.-L. et al., 2022, the main challenges in LST products can be summarized as: (1) Spatial discontinuity where values are missing in cloudy pixels due to the fact that TIR cannot penetrate clouds. (2) Spatiotemporal incomparability where each pixel in the scene has a different angle and local viewing time. (3) Short time span, as most of TIR data (except Landsat series data) are not available for a long time, which limits long time series analysis. (4) Instantaneity, where LST products are only available for the specific time when the satellite passes overhead [39]. In addition to these problems, data handling and interpretation problems arise. Indeed, because all satellite thermal data used in LST estimation are presented in coarse spatial resolution, this is the main challenge that faces many applications, such as thermal environment and UHI delineation, monitoring agricultural drought, and climate change research.

Understanding the relationship between land cover types and LST is therefore crucial for identifying LST's fine spatial resolution. For example, TIR sensors in the Landsat series collect TIR radiance emitted from the land surface in bands with a spatial resolution of approximately 100 m, which is then resampled to 30m. On the other hand, optical sensors provide high spatial resolution data (1.5 m Spot 7 data). On this basis, each pixel of TIRS data represents about 400 pixels of spot data. Each pixel may belong to a certain class of features that have a cooling or warming effect on the ambient surroundings. Several studies have investigated the relationship between land use land cover (LULC) and LST, focusing on how urban planning can mitigate urban UHI. For instance, Zhao et al. explored the effectiveness of cool and hot sources in either enhancing or mitigating LST under different temperature backgrounds, highlighting how different land uses such as water bodies, greenery, and developed areas affect temperature [47]. Similarly, He et al. used a concentric zonal analysis to investigate LULC-LST relationships in Shenyang, China, and found that buildings and roads are primary contributors to higher temperatures, while vegetation and water bodies act as cooling sources [48]. Other studies have employed the spatial grid as the analytic unit for correlations between land use indicators and LST [49,50].

This study aims to understand the intricate interaction of land cover types in terms of proportion, emissivity, and effect on LST calculation. The main objective of this paper is to develop a model to integrate high spatial resolution imagery (Spot 7 imagery) with the TIR data (Landsat 8), using the construction of land cover correspondence between the two datasets and neighborhood effects to produce reliable LST products with an acceptable resolution, which could help discover environmental thermal and developing solutions. The main contributions of this study can be summarized as follows:

- Designing, applying, and validating the model for integrating high-resolution images with TIR data to obtain high-resolution LST products.

- Correction of LST of Jeddah city, Saudi Arabia, extracted from Landsat 8 based on field measured of temperature in homogeneous regions.
- Using machine learning models to estimate the coefficients of cooling and heating for neighboring pixels of spot images based on the land cover type and the calculated and measured LST.

The paper's structure comprises the following sections: Section 2 covers materials and methods, including the study area and methodology. The results are presented in Section 3. Section 4 discusses the results and Section 5 presents the conclusions of this study.

2. Materials and Methods

2.1. Study Area

Jeddah city, as shown in Figure 1, is located on the west coast of Saudi Arabia (29.21° latitude, 39.7° longitude). It is considered the second-largest city in Saudi Arabia. The estimated population of Jeddah city was around 4.86 million people (about 14% of the total population of the Kingdom) in 2023 [51]. The urban area of Jeddah covers about 5460 km^2 [52]. The terrain elevations in Jeddah reach up to 265 m above the mean sea level. Unlike most cities in Saudi Arabia, Jeddah experiences an arid climate characterized by intense heat in the summer and mild warmth during the winter. Summer temperatures can soar above 48 °C in the afternoon and remain around 35 °C in the evening. In winter, temperatures typically range from 15 °C in the early morning to 28 °C in the afternoon. Two districts from the city of Jeddah were selected as case studies for this paper. The first is the Al Marjan district, a large, self-contained residential tourist resort offering various services and entertainment. Located in the northern part of Jeddah, it is one of the newly developed areas and was designed with a luxurious and upscale urban plan. The district features luxurious housing as well as entertainment and leisure facilities that make it one of the key contributors to tourism in Jeddah. The second is the Al-Hamra district, one of the oldest and most developed neighborhoods in the city, which may well have been the starting point for the urban development of the entire city. As a result, it has attracted the largest and most famous tourist landmarks in Jeddah, especially because it is a coastal district with Red Sea beaches stretching along its western borders. The selection of these two districts highlights their typicality and necessity, as they represent diverse land cover types and provide a balanced context for examining variations in LST.

2.2. Methodology

The Landsat 8 OLI/TIRS image captured on 7 May 2023 provided by the United States Geological Survey (USGS) was used in this study, along with the Spot 7 image captured that day, to explore the impact of LULC on LST over Jeddah city.

The proposed method can be summarized in the following steps: the first step is the land cover classification, where the high-resolution images from the SPOT 7 satellite and medium-resolution spatial images from the Landsat 8 satellite are classified using the optical bands. The second step is using the thermal band (band 10, Landsat 8) to estimate the initial LST over the study area. The third step is the correction of the calculated temperature using the measured data of homogeneous regions (HRs) of the selected area. The fourth step is developing a model using deep learning for temperature corrections, through which the calculated temperature is compared with the measured one. A workflow for the proposed method is depicted in Figure 2.

2.2.1. LULC Classification

To perform the LULC classification, a Landsat 8 image, which was captured in May 2023, as well as a Spot 7 image captured in the same week, were used. Supervised classification using the Random Forest algorithm was performed on the GEE platform to generate the LULC map for this image [53]. The Landsat 8 and Spot 7 images were categorized as one of five classes: urban, vegetation, roads, water, or barren lands. All residential, commercial, industrial, and other facilities related to urban infrastructure are

represented as urban class. Roads represent segments coated with asphalt in the study area. The vegetation class denotes all grass cover areas, agricultural lands, and trees, while the barren lands class refers to the city's non-inhabited areas. Water areas comprise wetland areas, lakes, ponds, and sea. To evaluate the accuracy of the LULC classification, a stratified random sampling approach was employed to select points within the study area. These points were then matched with independent reference datasets that were distinct from the data used for training during the image classification process. The number of selected validation points for each class was proportional to the relative size of that class, resulting in a total of 143 points distributed across the study areas. The reference data were validated on the field by measuring the true land surface temperature at these points. A confusion matrix was conducted using ENVI 5.3 software and used for statistical analysis to determine classification accuracy. The overall accuracy metric was employed to represent the classification accuracy achieved, while the Kappa coefficient was calculated to evaluate the level of agreement in class labeling.

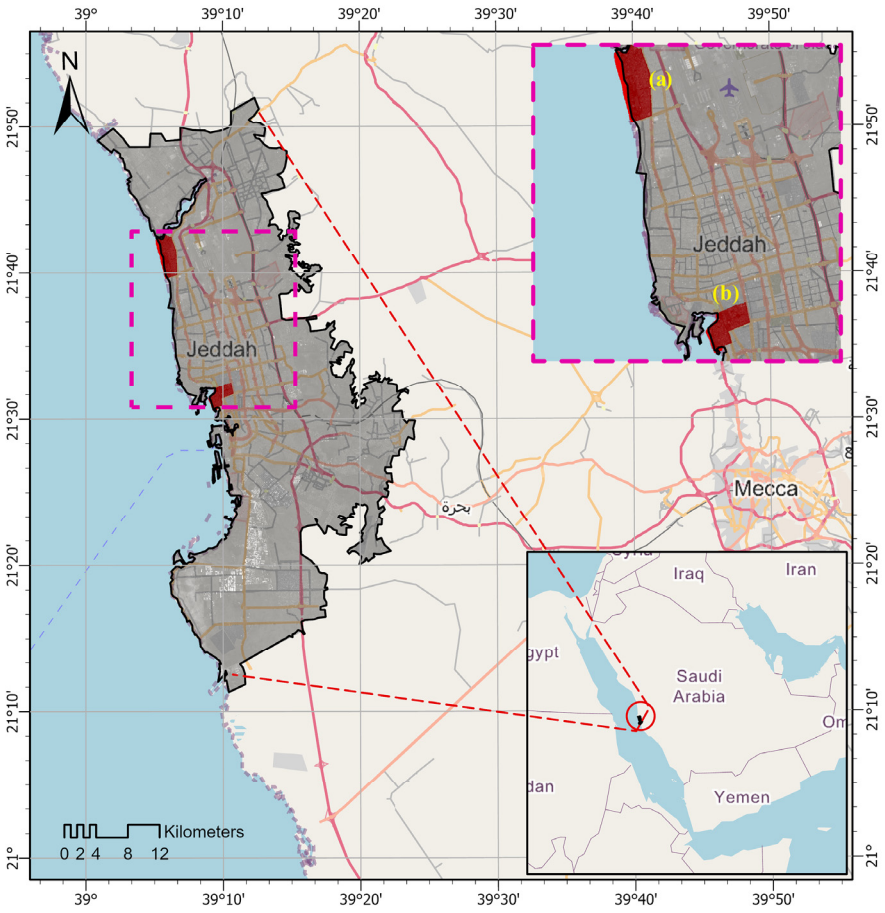

Figure 1. Location map of the study areas; (**a**) Al Marjan district, (**b**) Al Hamra district.

2.2.2. LST Retrieval Using Landsat 8 Imagery

In this research, thermal infrared band 10 from the Landsat 8 thermal infrared sensor (TIRS) was used to extract and map the LST of the study areas via the SC method. To mitigate atmospheric effects on the thermal infrared images, several assumptions were made using the ENVI 5.3 software: first, atmospheric conditions are assumed to be uniform across the entire data scene; second, consistent emissivity for all features is assumed; third, the reflected downwelling radiance is assumed to be absent; and fourth, the scene includes a near-blackbody surface.

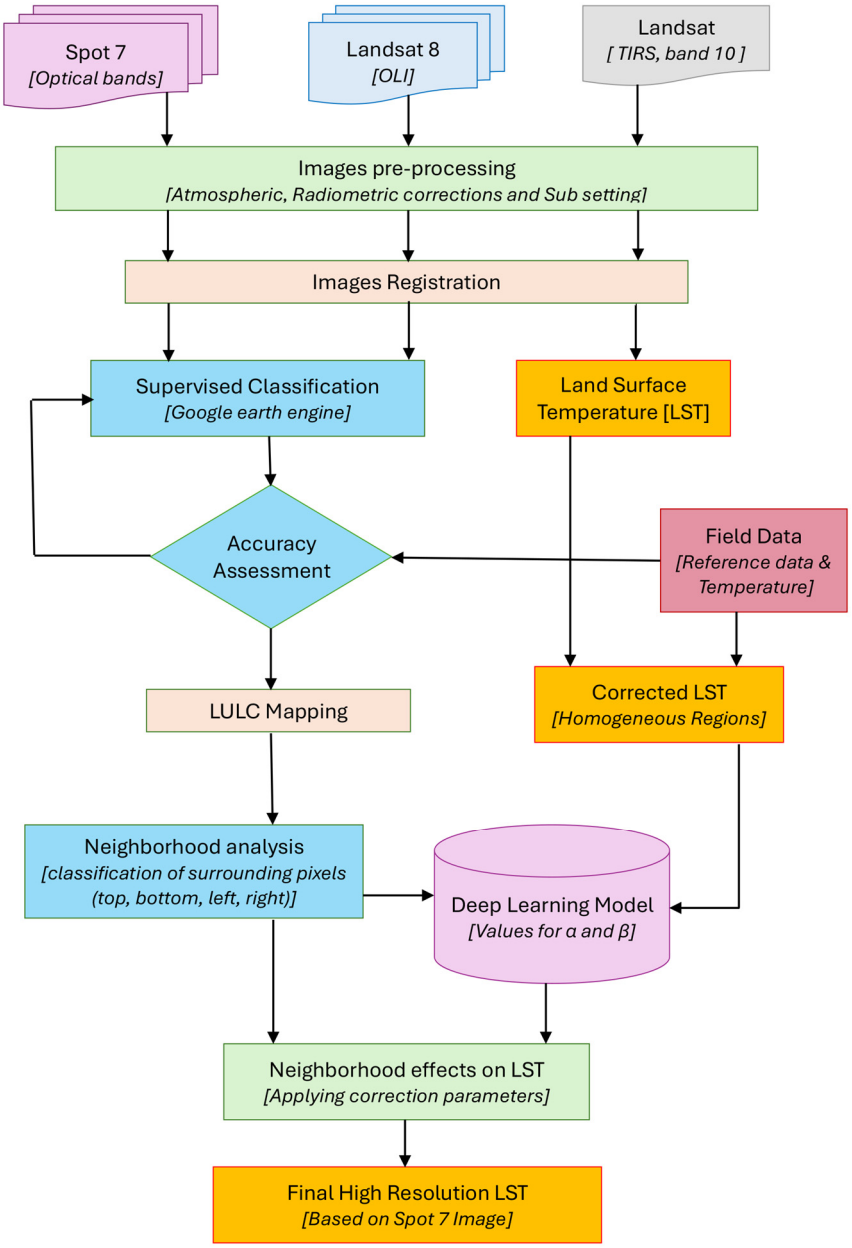

Figure 2. Workflow for the proposed method.

The process for extracting temperature values from the digital numbers (DNs) is detailed in the Landsat 8 User's Handbook [54] and involves several key steps. First, the DNs are converted to radiance using the following formula:

$$L_\lambda = M_L \times Q_{cal} + A_L \quad (1)$$

where L_λ is the Top of Atmosphere (TOA) radiance; M_L and A_L are the multiplicative and the additive scaling factors, respectively; and Q_{cal} is the image pixel value.

Then, the following formula can be used to obtain the effective at-satellite temperature from the above spectral radiance [55–57]:

$$T_B = \frac{K_2}{\ln(\frac{K_1}{L_\lambda} + 1)} \quad (2)$$

where T_B is the TOA brightness temperature, in Kelvin; L_λ is the spectral radiance; and K_1 and K_2 are the retrieved metadata's thermal conversion.

The LST can be derived from T_B if the emissivity values (ε) is determined using the following equation [58,59]:

$$\varepsilon = m\, P_v + n \tag{3}$$

where ε refers to the land surface emissivity, m = 0.986, P_v is the proportion of vegetation, and n = 0.004.

P_v can be calculated as Equation (4) [57,60]:

$$P_v = \left(\frac{NDVI_{max} - NDVI_{min}}{NDVI_{max} + NDVI_{min}}\right)^2 \tag{4}$$

$$\text{NDVI} = \frac{\rho_{NIR} - \rho_{RED}}{\rho_{NIR} + \rho_{RED}} \tag{5}$$

where ρ_{RED} is the surface reflectance of red band, and ρ_{NIR} is the surface reflectance of near infrared band. Finally, the LST in Celsius can be estimated using Equation (6):

$$\text{LST} = \left(\frac{T_B}{1 + \lambda\left(\frac{T_B}{\rho}\right)\ln(\varepsilon)}\right) - 273.15 \tag{6}$$

where λ is the wavelength of emitted radiance of Landsat 8, band 10; $\rho = h\left(\frac{c}{\sigma}\right)$, h is Planck's constant (6.626×10^{-34} Js); c is the velocity of light; and σ is Boltzmann constant (1.38×10^{-23} J/K).

2.2.3. Measuring the Actual Temperature in the Field

In this step, the LST is measured over the homogeneous regions (HRs) in the study areas. HRs refer to the areas where land cover classification matches between the high-resolution Spot image and the medium-resolution Landsat image. These areas are termed HRs for each of the five classification categories. They ensure consistency in classification despite spatial resolution differences. The temperature was measured over 133 different points distributed over the study areas: 32 in urban HRs, 39 in roads, 37 in vegetation HRs, 18 in HRs of barren lands, and 7 in water HRs.

2.2.4. Temperature Correction Model

The measured temperature data at HRs only for the five classification categories are used to rescale the calculated temperature using the single window algorithm for the Landsat thermal image, according to the following equation:

$$LST_{Corr} = LSTE\left(\frac{LSTM_{max} - LSTM_{min}}{LSTE_{max} - LSTE_{min}}\right) \tag{7}$$

where $LSTE$ refers to the estimated LST from the Landsat image and $LSTM$ refers to the measured in field LST.

After applying the correction, almost all errors are assumed to be eliminated and the LST values from Landsat are corrected using the actual temperature values of HRs for each class. Then, the corrected LST image is linked with the fine land cover classification that comes from Spot image to identify the temperature values for heterogeneous regions. To determine the temperature values for heterogeneous regions—basically, to study the effect of the neighborhood, i.e., each pixel in the high-resolution image—the influence of the surrounding four pixels (top, bottom, left, right) is studied and influence parameters are determined based on classification. Influence parameters are determined as: α/alpha for increasing temperature if the neighboring pixel is classified as buildings, barren lands, or roads, and β/beta for decreasing temperature if the neighboring pixel is classified as

vegetation or water. No influence (coefficient of 1) is applied if the neighboring pixel has the same classification. To do so, the following procedure is followed:

(1) Each Spot-classified image pixel is assigned an initial temperature based on the closest homogeneous region of its classification category.
(2) Influence parameters for each pixel based on the neighborhood analysis are assigned.
(3) The average temperature for each Spot region covering a Landsat pixel is calculated, considering the influence coefficients α and β.
(4) The best values for α and β are determined using the corrected Landsat temperature image and a machine learning model.
(5) The actual temperature for each Spot image pixel is calculated.

The actual temperature at the Spot pixel level can be calculated as follows:

$$T_{act} = LST_{Corr} \times \alpha^m \times \beta^n \quad (8)$$

where T_{act} is the actual temperature at Spot pixel level, LST_{Corr} is the corrected LST, α and β are the heating and cooling coefficients, m is the number of heating pixels and n is the number of cooling pixels within one Landsat pixel.

3. Results

3.1. Classification of Images and Accuracy Assessment

As mentioned in Section 2.2.1, the study area is divided into five classes from both Landsat and Spot images: urban, roads, vegetation, barren lands, and water. The classified images of the Al Marjan and Al Hamra districts are presented in Figures 3 and 4 and quantified in Table 1. From the figures, it is clear that spatial resolution plays a crucial role in achieving reliable classification. The classification results of Spot images are more precise than those of Landsat images. Regarding the accuracy assessment results, Table 2 summarizes the accuracy assessment results evaluated using a confusion matrix for the LULC classification of the two regions selected. Approximately 15 sampling points for each class were selected randomly and then compared with the selected reference data based on Google Earth imagery. The overall accuracy achieved ranged from 93% to 95% for Spot images, while it was never better than 77% for Landsat images. The Kappa coefficients as indicators of agreement in class labeling for all classifications were 0.791 and 0.882 for the Al Marjan district, and 0.802 and 0.894 for the Al Hamra district, for the Landsat and Spot images, respectively.

Table 1. LULC distribution over the study area.

Image		Urban		Roads		Vegetation		Barren Lands		Water	
		Area (km^2)	Area%	Area (km^2)	Area%	Area (km^2)	Area%	Area (km^2)	Area%	Area (km^2)	Area%
Al Marjan	Landsat	2.586	24.98%	1.185	11.45%	3.479	33.61%	2.131	20.59%	0.970	09.37%
	Spot	2.153	20.72%	3.922	37.75%	1.536	14.79%	1.561	15.02%	1.218	11.73%
Al Hamra	Landsat	1.533	25.90%	2.844	42.03%	0.952	10.09%	0.524	08.85%	0.422	07.13%
	Spot	1.069	18.15%	2.837	48.15%	0.735	12.47%	0.881	14.95%	0.370	06.28%

Table 2. Accuracy assessment for LULC classification.

Classification		Overall Accuracy	Kappa Coefficient
Al Marjan	Landsat	74%	0.791
	Spot	93%	0.882
Al Hamra	Landsat	77%	0.802
	Spot	95%	0.894

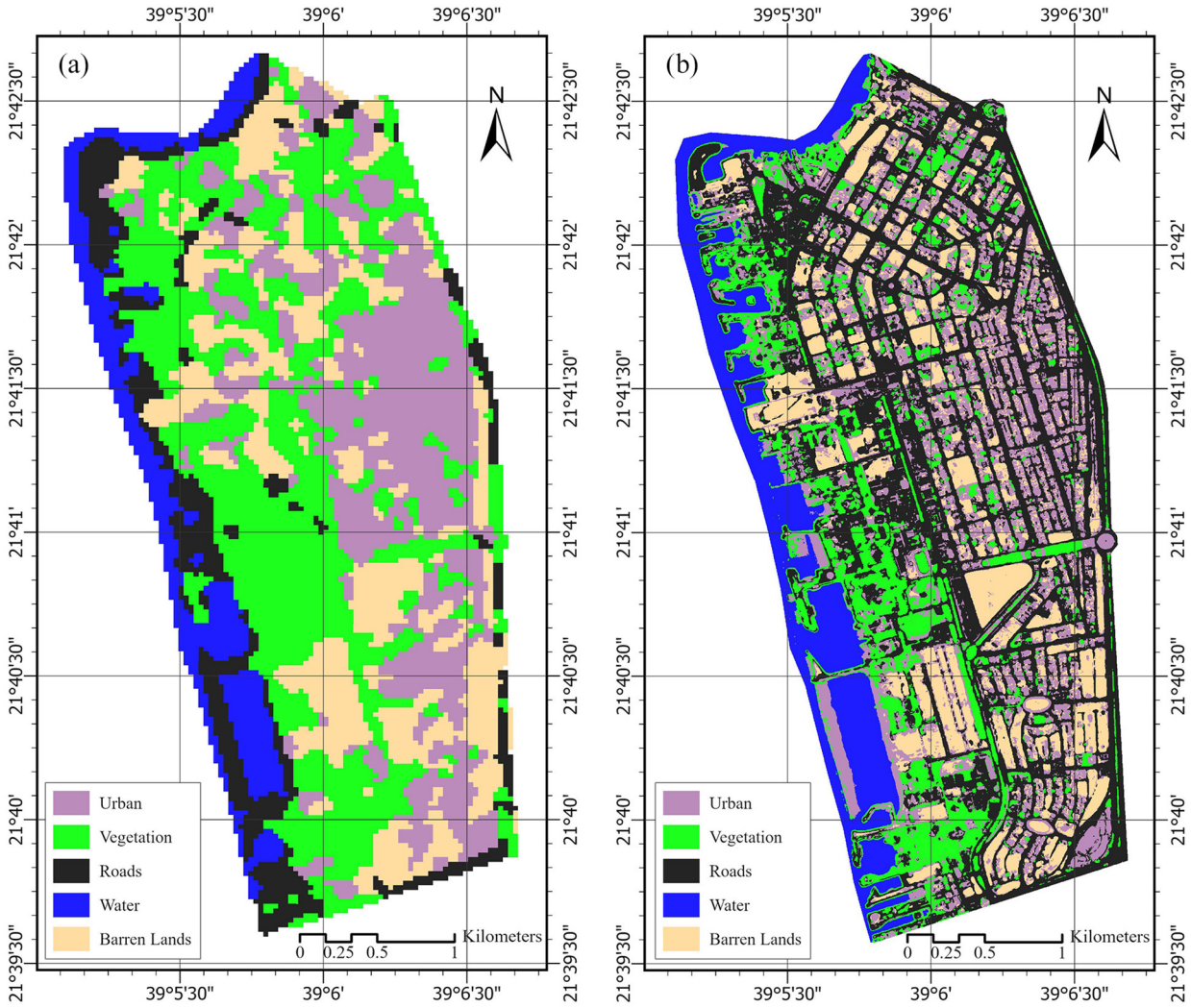

Figure 3. Spatial LULC in the Al Marjan district of Jeddah city in 2023; (**a**) Landsat 8, (**b**) Spot 7.

3.2. LST Spatial Distribution

The spatial distribution of LST in Jeddah on 7 May 2023 over the selected districts was extracted from Landsat 8 imagery using the procedure mentioned in Section 2.2.2 and depicted in Figure 5. Table 3 presents the descriptive statistics for LST distribution over each land class. The results indicate the ranges of LST for different classes as follows: In the Al Marjan district, 31.3–39.5 °C, 28.7–40.3 °C, 30.0–40.2 °C, 27.1–32.2 °C, and 31.6–40.0 °C and in the Al Hamra district, 33.0–40.6 °C, 30.5–39.4 °C, 31.4–40.0 °C, 28.2–34.5 °C, and 32.4–41.0 °C for urban, vegetation, roads, water, and barren lands, respectively. Figure 6 presents boxplots to gain a deeper insight into the spatial distribution of LST for each class over the study areas. Table 4 shows a comparison between temperature value ranges for each class between the calculated values and those measured in the field. A significant discrepancy between the corresponding values was observed.

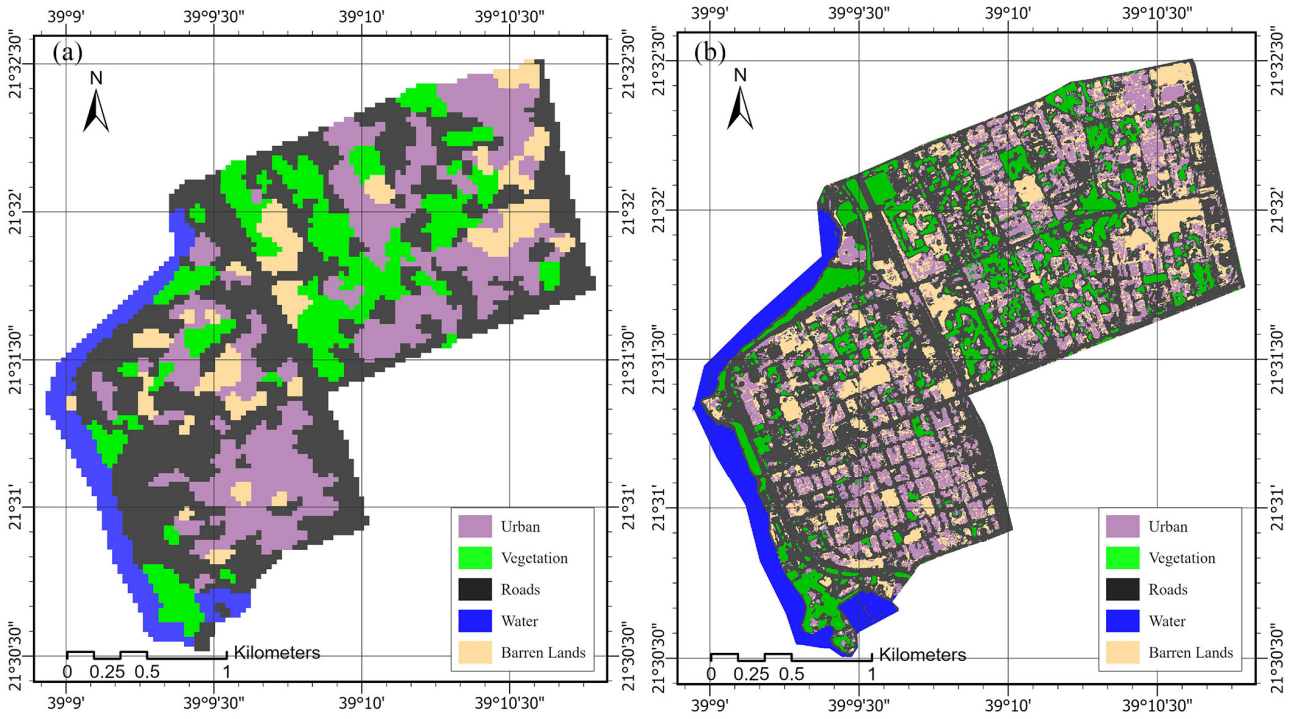

Figure 4. Spatial LULC in the Al Hamra district of Jeddah city in 2023; (**a**) Landsat 8, (**b**) Spot 7.

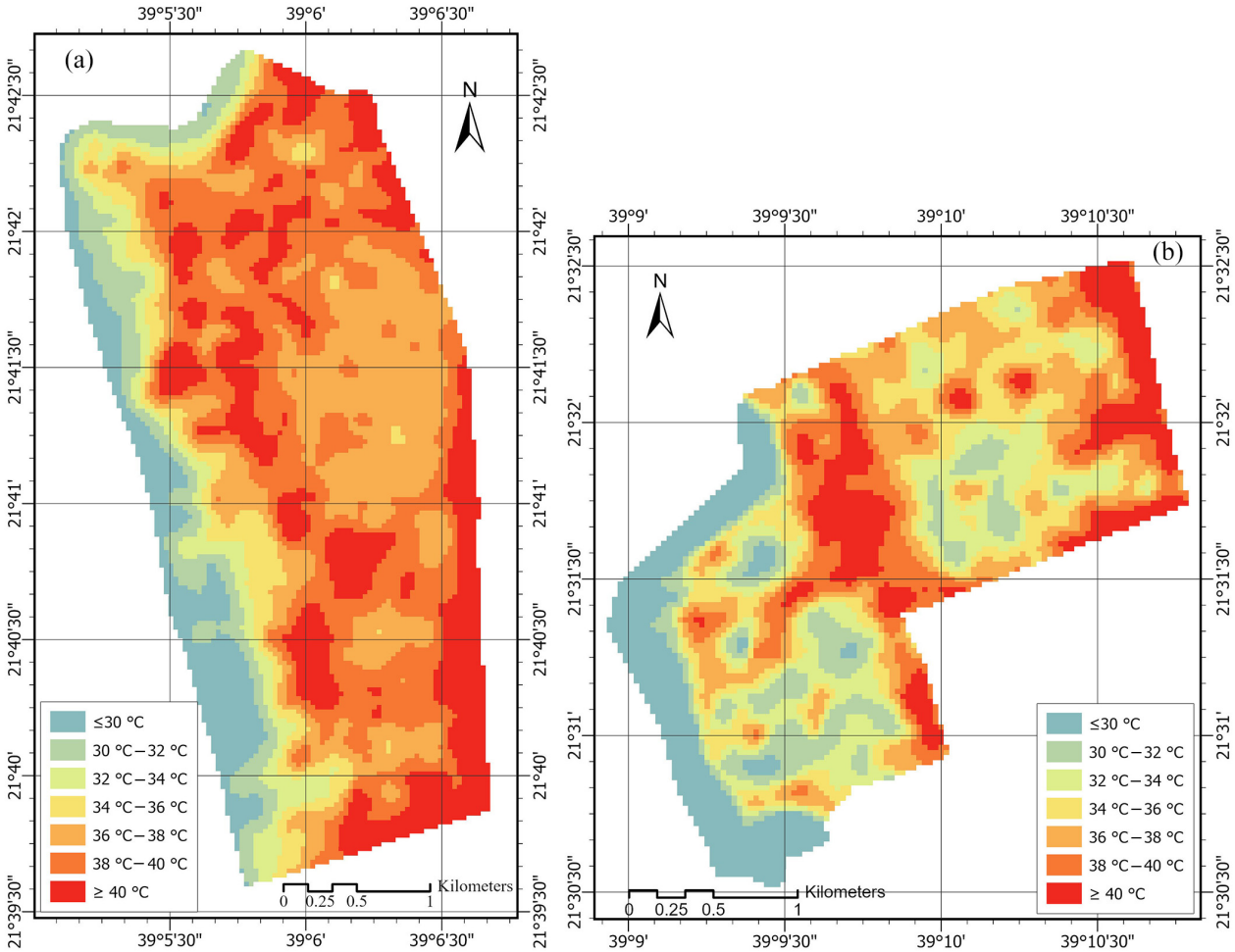

Figure 5. Spatial distribution of LST in (**a**) the Al Marjan and (**b**) Al Hamra districts of Jeddah city.

Table 3. Descriptive statistics of LST for the LULC of the study areas.

Land Cover		Min. (°C)	Mean (°C)	Max. (°C)	Median (°C)	S.D. (°C)
Urban	Al Marjan	31.3	36.8	39.5	36.7	0.94
	Al Hamra	33.0	37.2	40.6	37.1	0.88
Vegetation	Al Marjan	28.7	36.2	40.3	36.6	2.02
	Al Hamra	30.5	36.6	39.4	36.9	1.59
Roads	Al Marjan	30.0	34.6	40.2	33.6	3.44
	Al Hamra	31.4	37.8	40.0	37.7	1.10
Water	Al Marjan	27.1	28.6	32.2	28.4	0.96
	Al Hamra	28.2	30.1	34.5	29.9	1.29
Barren lands	Al Marjan	31.6	38.1	40.0	38.2	0.95
	Al Hamra	32.4	38.4	41.0	38.5	1.16

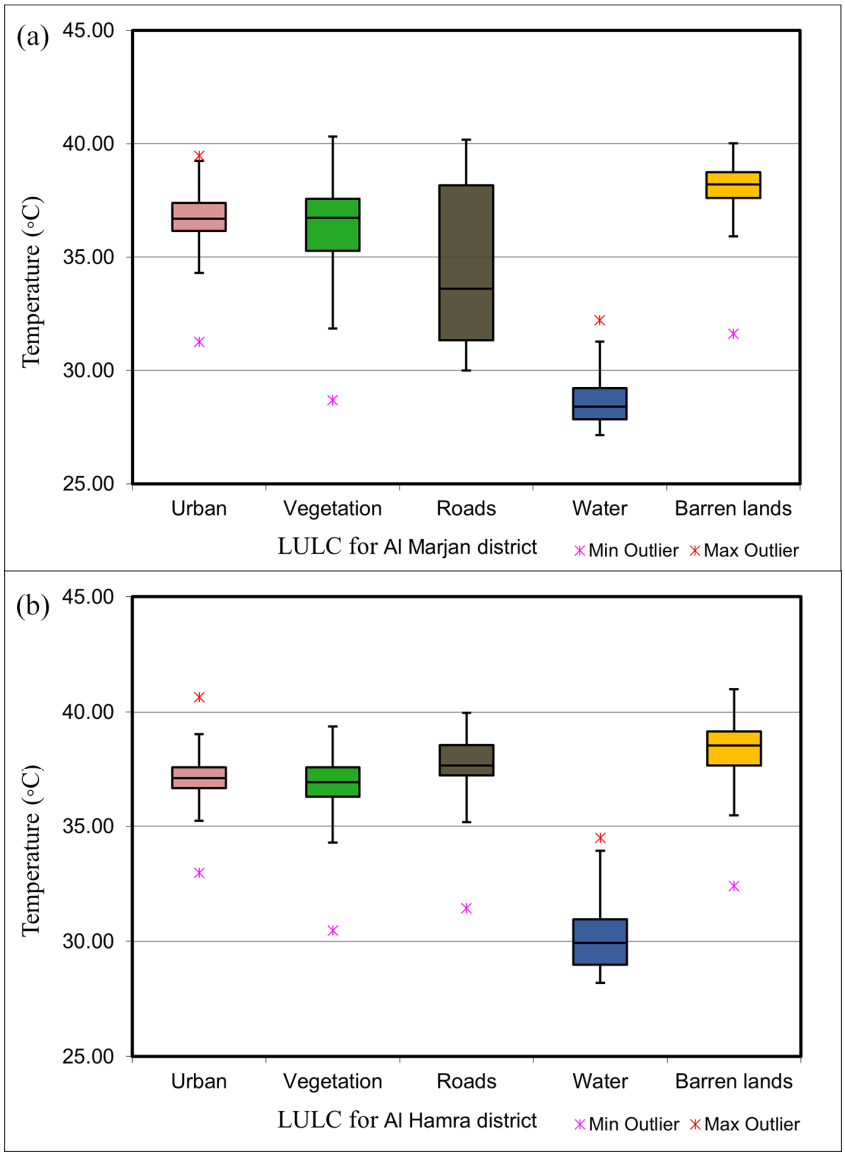

Figure 6. Boxplot showing the spatial distribution of LST based on Landsat image classification in (**a**) the Al Marjan and (**b**) Al Hamra districts of Jeddah city.

Table 4. Comparison between LST ranges estimated from Landsat 8 image and those measured in the field for different LULC classes.

Land Cover	LST Range Estimated Image (°C)	LST Range Measured in the Field (°C)
Urban	31.3–40.6	33.5–42.0
Vegetation	28.7–40.3	31.5–41.5
Roads	31.4–40.2	35.5–44.0
Water	27.1–34.5	29.0–32.0
Barren lands	31.6–41.0	36.0–44.5

3.3. LST Correction

Differences between the calculated LST from the Landsat image and measured LST ranges are presented in Table 4. Many factors contribute to these errors, including atmospheric effects, the emissivity of different objects, and the time difference between field measurements and image capturing. To eliminate these errors, the LST extracted from Landsat 8 image is based on Equation (7) and the true measured data over the HRs.

3.3.1. Calculating the Cooling and Heating Coefficients

Each pixel in the Landsat classified image covers about 400 pixels of the Spot classified image (1.5 m spatial resolution), which includes cooling and heating pixels. Using the Landsat corrected temperature, an initial temperature is assigned to each Spot pixel based on the closest homogeneous region of the same class of pixel. The average LST of 400 pixels of Spot image should equal to the value of LST of the Landsat pixel that covers the same area, taking into account the cooling and heating effects. Table 5 shows the data related to the Landsat pixels temperatures and their corresponding Spot pixel counts, i.e., the number of heating and cooling pixels as well as the number of neutral pixels. A linear regression model was trained to find a suitable heating and cooling coefficient based on the number of heating and cooling pixels at the same average temperature level. The value of heating coefficient α is about 1.06 and cooling coefficient β is about 0.96.

Table 5. Landsat pixel temperatures and their corresponding Spot pixel counts.

LST (°C)	Number of Spot Neutral Pixels/Landsat Pixel	Number of Spot Heating Pixels/Landsat Pixel	Number of Spot Cooling Pixels/Landsat Pixel
36.27	359	29	10
36.27	351	43	6
37.16	352	29	19
38.36	351	36	13
39.43	358	25	17
39.43	346	37	17
40.42	371	16	13
41.15	357	29	14
41.71	345	40	15
42.26	352	30	18

3.3.2. Neighboring Pixels Effect on LST

To study heat transfer between adjacent pixels and determine the neighboring effect, a new high-resolution raster with five bands for each study area was created based on Spot image classification. The pixel's classification is represented in the first band, the second band shows the classification of the pixel above, the third band shows the classification of the pixel below, and the fourth and fifth bands represent the classifications of the pixels to the left and right, respectively. This new raster is linked to the corrected Landsat 8 LST, as discussed in Section 2.2.4, to calculate the neighboring pixels effect. Figure 7 depicts the workflow of enhancing LST via Spot imagery.

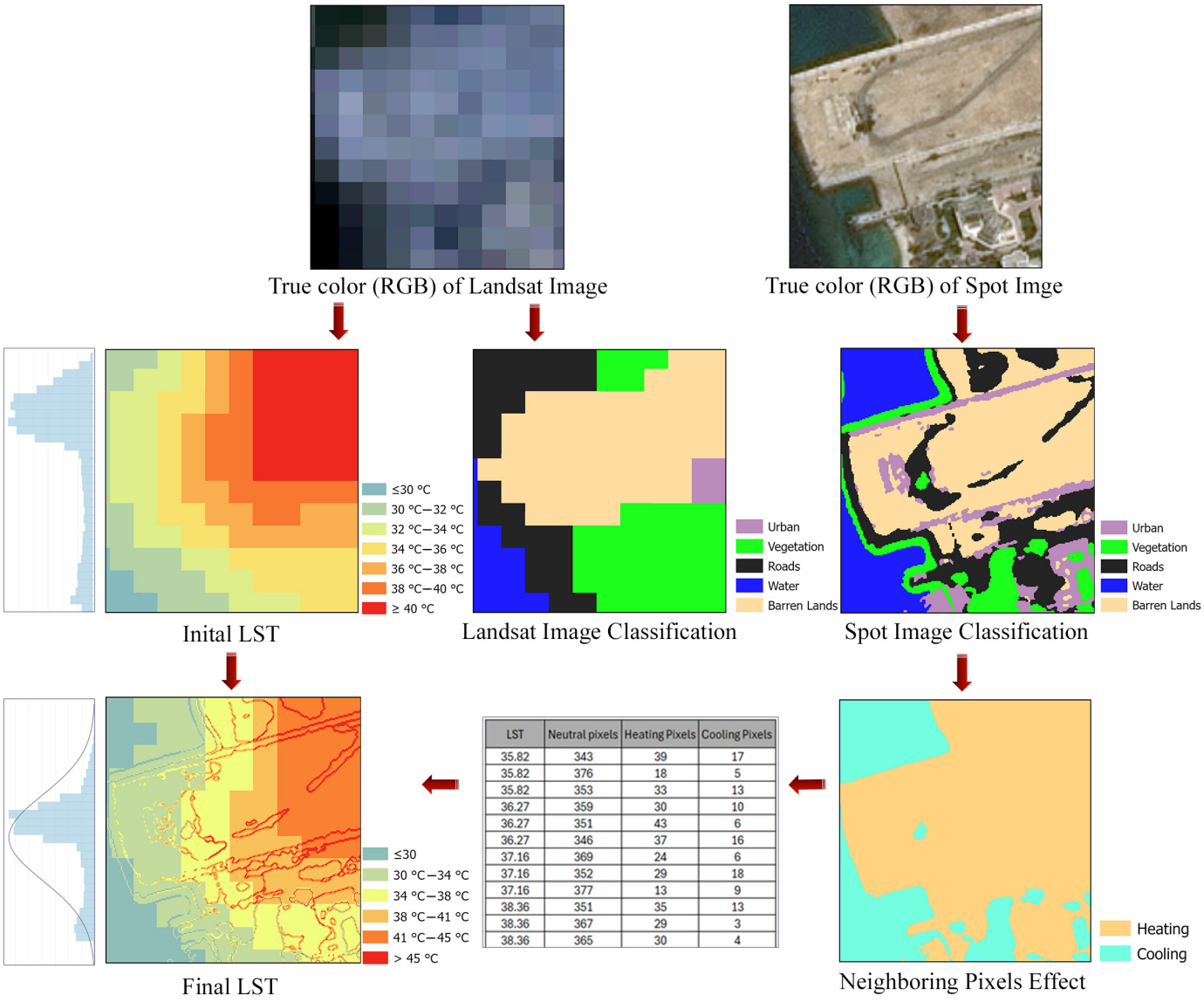

Figure 7. The workflow of enhancing LST via Spot imagery.

Figure 8 shows the spatial distribution of the final LST at the Spot pixel level. The LST for all LULC classes were enhanced. Figure 9 presents a boxplot for the spatial distribution of the enhanced LST and in Table 6, the comparison between the mean values of LST before and after enhancement are presented. For the Al Morjan district, the water class has the lowest median indicator of about 28.2 °C followed by roads, vegetation, and then urban; the highest median was recorded in barren lands at 38.3 °C. The range of temperature of the roads class was the largest with a range of about 17.8 °C, followed by vegetation, urban, and barren land. The water class had the smallest range, which was 6.6 °C.

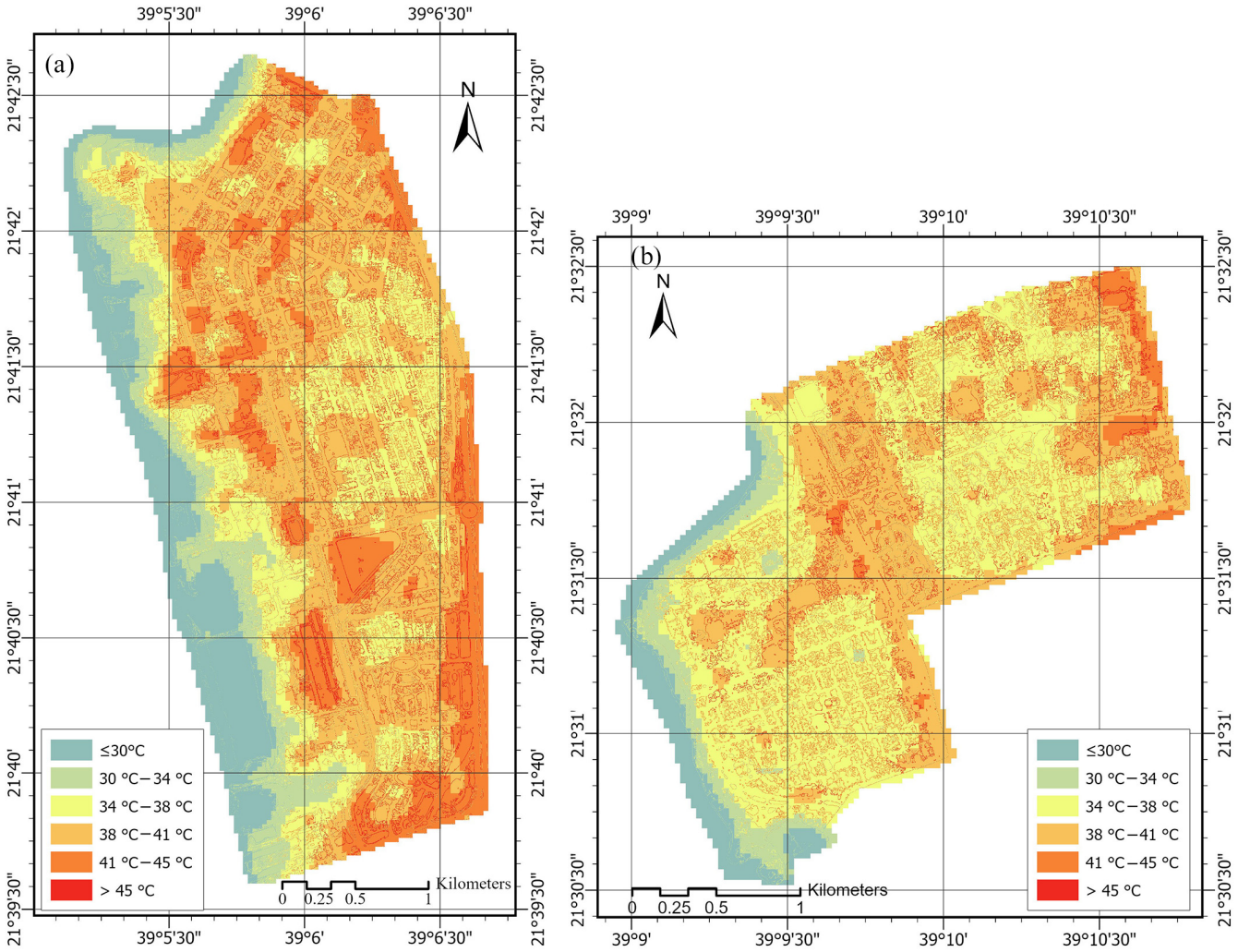

Figure 8. Spatial distribution of the final LST in (**a**) the Al Marjan and (**b**) Al Hamra districts of Jeddah city. Boxplots for water urban and barren lands seem to be not skewed, while boxplots for roads and vegetation appear to be skewed right. In the Al Hamra district, the lowest median value (29.6 °C) was in water. The median values for vegetation, urban, roads, and barren lands were 37.1 °C, 37.2 °C, 37.6 °C, and 38.8 °C, respectively. However, this comparison may be less informative about dispersion than comparing the lengths of the boxes, due to the presence of potential outliers in all datasets.

Table 6. Comparison between mean values of LST (°C) before and after enhancement.

		Urban	Vegetation	Roads	Water	Barren Lands
Al Marjan	Initial LST	36.8	36.2	34.6	28.6	38.1
	Final LST	38.2	37.4	38.0	29.0	39.1
Al Hamra	Initial LST	37.2	36.6	37.8	30.1	38.4
	Final LST	38.6	38.0	38.9	30.5	39.6

The results clearly show that the spatial distribution of the temperature values was enhanced, and the mean values of all classes' temperatures increased.

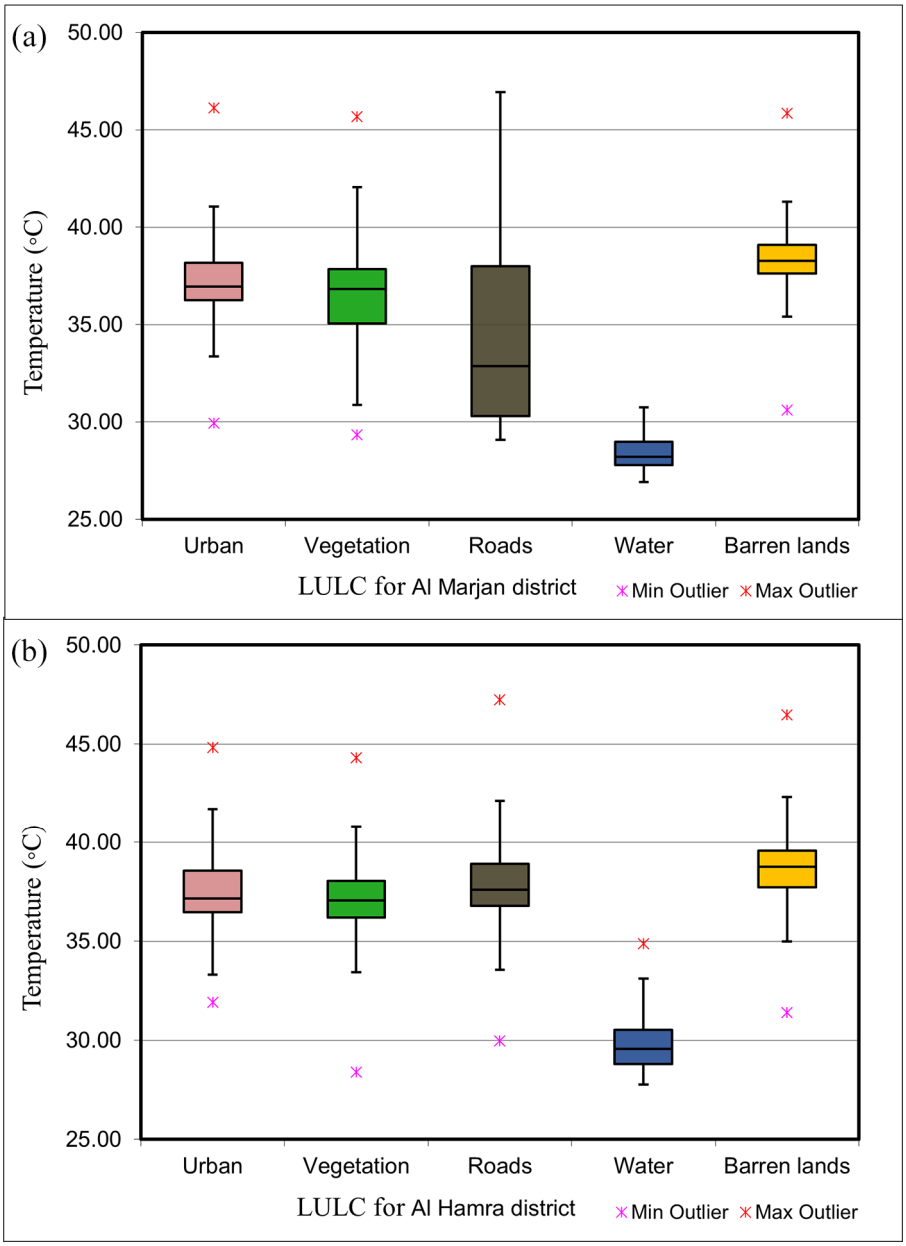

Figure 9. Boxplot for spatial distribution of the final temperature in (**a**) the Al Marjan and (**b**) Al Hamra districts of Jeddah city.

4. Discussion

Obtaining a high-resolution LST map is crucial for accurately managing various environmental and urban challenges. It provides detailed insights into localized temperature variations, enabling a better understanding and delineation of heat islands, microclimate conditions, and their impacts on urban planning, agriculture, and ecosystems. This paper presents a new method for obtaining high-resolution LST. The proposed method does not require prior deep knowledge about the study area, and no extra parameters such as LSE or atmosphere transmittance are needed. Only the thermal band data and a high-resolution image are the input parameters.

The classification results of Landsat 8 and Spot imagery and corresponding quantifications revealed that spatial resolution plays a crucial role in obtaining reliable classifications. This finding is further reinforced by the accuracy assessment, which shows that Spot images achieved an overall accuracy of over 95%, while Landsat images did not exceed 77%. The Kappa coefficients also reflected higher agreement for Spot images, indicating that

high-resolution images provide more reliable LULC classification, especially in complex urban environments. This supports the argument that high-resolution images, like those from Spot 7, are better suited for detailed studies related to image classification.

In addition to the cooling and heating coefficients, the study also examined the influence of neighboring pixels on LST values. The results demonstrated that the spatial distribution of LST improved, with overall temperature increases observed across all land-cover classes in the study areas. In the Al Marjan and Al Hamra districts of Jeddah, temperature variability was most pronounced in road areas, reflecting higher fluctuation. This can be attributed to the nature of roads, which traverse the entire study area and are adjacent to different land-cover types with varying temperatures. As expected, water remained the coolest class, while barren lands were the hottest. The analysis of neighboring pixels offered further insights into how adjacent land-cover types affect temperature patterns, underscoring the importance of spatial resolution and localized interactions when studying LST.

Our findings highlight the importance of high-resolution imagery in improving the accuracy and reliability of LULC classification and LST modeling. The enhanced spatial resolution provided by Spot images allowed for more precise temperature estimations and a better understanding of the thermal interactions between different land-cover types. The study also underscored the significance of accounting for neighboring pixel effects and correcting LST data to reduce discrepancies between satellite-derived and field-measured temperatures. These results have important implications for UHI studies, environmental monitoring, and sustainable urban planning.

In comparison with the previous studies, this study confirms that LULC types significantly influence LST, with urban areas such as roads and barren lands contributing to elevated temperatures, whereas vegetation and water bodies act as cooling sources. The same results were achieved in [49,50]. Furthermore, our study introduces heating and cooling coefficients to quantify neighboring pixel effects, an approach that enhances the precision of LST calculations and offers a novel perspective on how localized configuration of LULC influences temperature.

Some limitations arose in this study. First, the field temperature data collecting time was not the same as the time of capturing the satellite image. Second, the heating and cooling coefficients in this study are assumed to be constant for all classes, however, this is not true, and they can vary from class to class.

Future research could yield more insights by investigating the heating and cooling coefficients for different LULCs and examining the use of very high-resolution images.

5. Conclusions

This study was motivated by the need for high-resolution LST products to be used in different applications, such as UHI delineation, environmental monitoring, and sustainable urban planning. We therefore proposed a new method, which is also a general framework, to systematically retrieve fine resolution LST. This method integrates high and medium-resolution satellite data to improve temperature estimation spatial accuracy. Landsat 8 and Spot 7 imagery for two districts, Al Morjan and Al Hamra in Jeddah, Saudi Arabia, were used in this research as a case study. The estimated LST from the Landsat thermal band was corrected via field measurements and the classification output of the fine resolution image was integrated with the corrected LST. The study also examined the influence of neighboring pixels on LST values and quantified the heating and cooling coefficients used to enhance them. A machine learning model was used to quantify the contribution of each Spot pixel to the LST estimated from TIRS data and classified as heating or cooling. The value of the heating coefficient for pixels in the classes of urban, roads, and barren lands was 1.06, and while the value of cooling coefficient for pixels of vegetation and water was 0.96. The results highlighted spatial resolution's crucial role in classification accuracy and reliability. The resultant LSTs for the two districts were enhanced completely. The barren lands recorded the hottest temperatures while water remained the coolest

class. The temperature variability was most pronounced in road class. The findings have implications for all applications utilizing LST on a regional and global scale. Future research should explore the application of this approach across diverse environments and use very high-resolution data to further enhance LST estimation accuracy.

Funding: This research work was funded by Institutional Fund Projects under Grant No. IFPIP-1203-137-1443 provided by the Ministry of Education and King Abdulaziz University, DSR, Jeddah, Saudi Arabia.

Institutional Review Board Statement: Not applicable.

Informed Consent Statement: Not applicable.

Data Availability Statement: The data that support the findings of this study are available on request from the corresponding author. The data are not publicly available due to privacy.

Acknowledgments: The author gratefully acknowledges the technical and financial support provided by the Ministry of Education and King Abdulaziz University, DSR, Jeddah, Saudi Arabia.

Conflicts of Interest: The author declares no conflict of interest.

References

1. Dash, P.; Göttsche, F.-M.; Olesen, F.-S.; Fischer, H. Land Surface Temperature and Emissivity Estimation from Passive Sensor Data: Theory and Practice-Current Trends. *Int. J. Remote Sens.* **2002**, *23*, 2563–2594. [CrossRef]
2. Li, Z.-L.; Tang, B.-H.; Wu, H.; Ren, H.; Yan, G.; Wan, Z.; Trigo, I.F.; Sobrino, J.A. Satellite-Derived Land Surface Temperature: Current Status and Perspectives. *Remote Sens. Environ.* **2013**, *131*, 14–37. [CrossRef]
3. Friedl, M.; Strahler, A. A Kernel-Driven Model of Effective Directional Emissivity for Non-Isothermal Surfaces. *Prog. Nat. Sci.* **2002**, *12*, 603–607.
4. Vancutsem, C.; Ceccato, P.; Dinku, T.; Connor, S.J. Evaluation of MODIS Land Surface Temperature Data to Estimate Air Temperature in Different Ecosystems over Africa. *Remote Sens. Environ.* **2010**, *114*, 449–465. [CrossRef]
5. Xu, T.; Guo, Z.; Xia, Y.; Ferreira, V.G.; Liu, S.; Wang, K.; Yao, Y.; Zhang, X.; Zhao, C. Evaluation of Twelve Evapotranspiration Products from Machine Learning, Remote Sensing and Land Surface Models over Conterminous United States. *J. Hydrol.* **2019**, *578*, 124105. [CrossRef]
6. Xu, T.; He, X.; Bateni, S.M.; Auligne, T.; Liu, S.; Xu, Z.; Zhou, J.; Mao, K. Mapping Regional Turbulent Heat Fluxes via Variational Assimilation of Land Surface Temperature Data from Polar Orbiting Satellites. *Remote Sens. Environ.* **2019**, *221*, 444–461. [CrossRef]
7. Tajfar, E.; Bateni, S.M.; Lakshmi, V.; Ek, M. Estimation of Surface Heat Fluxes via Variational Assimilation of Land Surface Temperature, Air Temperature and Specific Humidity into a Coupled Land Surface-Atmospheric Boundary Layer Model. *J. Hydrol.* **2020**, *583*, 124577. [CrossRef]
8. Menon, S.; Akbari, H.; Mahanama, S.; Sednev, I.; Levinson, R. Radiative Forcing and Temperature Response to Changes in Urban Albedos and Associated CO_2 Offsets. *Environ. Res. Lett.* **2010**, *5*, 014005. [CrossRef]
9. Fu, P.; Weng, Q. A Time Series Analysis of Urbanization Induced Land Use and Land Cover Change and Its Impact on Land Surface Temperature with Landsat Imagery. *Remote Sens. Environ.* **2016**, *175*, 205–214. [CrossRef]
10. Peng, J.; Ma, J.; Liu, Q.; Liu, Y.; Hu, Y.; Li, Y.; Yue, Y. Spatial-Temporal Change of Land Surface Temperature across 285 Cities in China: An Urban-Rural Contrast Perspective. *Sci. Total Environ.* **2018**, *635*, 487–497. [CrossRef]
11. Masoudi, M.; Tan, P.Y. Multi-Year Comparison of the Effects of Spatial Pattern of Urban Green Spaces on Urban Land Surface Temperature. *Landsc. Urban. Plan.* **2019**, *184*, 44–58. [CrossRef]
12. Miky, Y.H. Remote Sensing Analysis for Surface Urban Heat Island Detection over Jeddah, Saudi Arabia. *Appl. Geomat.* **2019**, *11*, 243–258. [CrossRef]
13. Wu, C.; Li, J.; Wang, C.; Song, C.; Chen, Y.; Finka, M.; La Rosa, D. Understanding the Relationship between Urban Blue Infrastructure and Land Surface Temperature. *Sci. Total Environ.* **2019**, *694*, 133742. [CrossRef] [PubMed]
14. Alexander, C. Normalised Difference Spectral Indices and Urban Land Cover as Indicators of Land Surface Temperature (LST). *Int. J. Appl. Earth Obs. Geoinf.* **2020**, *86*, 102013. [CrossRef]
15. Miky, Y.; Al Shouny, A.; Abdallah, A. Studying the Impact of Urban Management Strategies and Spatiotemporal Dynamics of LULC on Land Surface Temperature and SUHI Formation in Jeddah, Saudi Arabia. *Sustainability* **2023**, *15*, 15316. [CrossRef]
16. Bechtel, B. A New Global Climatology of Annual Land Surface Temperature. *Remote Sens.* **2015**, *7*, 2850–2870. [CrossRef]
17. Bright, R.M.; Davin, E.; O'Halloran, T.; Pongratz, J.; Zhao, K.; Cescatti, A. Local Temperature Response to Land Cover and Management Change Driven by Non-Radiative Processes. *Nat. Clim. Chang.* **2017**, *7*, 296–302. [CrossRef]
18. Tran, D.X.; Pla, F.; Latorre-Carmona, P.; Myint, S.W.; Caetano, M.; Kieu, H.V. Characterizing the Relationship between Land Use Land Cover Change and Land Surface Temperature. *ISPRS J. Photogramm. Remote Sens.* **2017**, *124*, 119–132. [CrossRef]

19. Cai, M.; Ren, C.; Xu, Y.; Lau, K.K.-L.; Wang, R. Investigating the Relationship between Local Climate Zone and Land Surface Temperature Using an Improved WUDAPT Methodology—A Case Study of Yangtze River Delta, China. *Urban. Clim.* **2018**, *24*, 485–502. [CrossRef]
20. Keenan, T.F.; Riley, W.J. Greening of the Land Surface in the World's Cold Regions Consistent with Recent Warming. *Nat. Clim. Chang.* **2018**, *8*, 825–828. [CrossRef]
21. Shen, Y.; Shen, H.; Cheng, Q.; Zhang, L. Generating Comparable and Fine-Scale Time Series of Summer Land Surface Temperature for Thermal Environment Monitoring. *IEEE J. Sel. Top. Appl. Earth Obs. Remote Sens.* **2021**, *14*, 2136–2147. [CrossRef]
22. Colliander, A.; Fisher, J.B.; Halverson, G.; Merlin, O.; Misra, S.; Bindlish, R.; Jackson, T.J.; Yueh, S. Spatial Downscaling of SMAP Soil Moisture Using MODIS Land Surface Temperature and NDVI During SMAPVEX15. *IEEE Geosci. Remote Sens. Lett.* **2017**, *14*, 2107–2111. [CrossRef]
23. Tang, R.; Li, Z.-L. An End-Member-Based Two-Source Approach for Estimating Land Surface Evapotranspiration From Remote Sensing Data. *IEEE Trans. Geosci. Remote Sens.* **2017**, *55*, 5818–5832. [CrossRef]
24. Tang, R.; Li, Z. Estimating Daily Evapotranspiration From Remotely Sensed Instantaneous Observations With Simplified Derivations of a Theoretical Model. *J. Geophys. Res. Atmos.* **2017**, *122*, 10–177. [CrossRef]
25. Gallego-Elvira, B.; Taylor, C.M.; Harris, P.P.; Ghent, D. Evaluation of Regional-Scale Soil Moisture-Surface Flux Dynamics in Earth System Models Based on Satellite Observations of Land Surface Temperature. *Geophys. Res. Lett.* **2019**, *46*, 5480–5488. [CrossRef]
26. Zhao, W.; Wen, F.; Wang, Q.; Sanchez, N.; Piles, M. Seamless Downscaling of the ESA CCI Soil Moisture Data at the Daily Scale with MODIS Land Products. *J. Hydrol.* **2021**, *603*, 126930. [CrossRef]
27. Lenschow, D.H.; Dutton, J.A. Surface Temperature Variations Measured from an Airplane over Several Surface Types. *J. Appl. Meteorol.* **1964**, *3*, 65–69. [CrossRef]
28. Price, J.C. Land Surface Temperature Measurements from the Split Window Channels of the NOAA 7 Advanced Very High Resolution Radiometer. *J. Geophys. Res. Atmos.* **1984**, *89*, 7231–7237. [CrossRef]
29. Ottlé, C.; Vidal-Madjar, D. Estimation of Land Surface Temperature with NOAA9 Data. *Remote Sens. Environ.* **1992**, *40*, 27–41. [CrossRef]
30. Li, Z.-L.; Becker, F. Feasibility of Land Surface Temperature and Emissivity Determination from AVHRR Data. *Remote Sens. Environ.* **1993**, *43*, 67–85. [CrossRef]
31. Sobrino, J.A.; Li, Z.-L.; Stoll, M.P.; Becker, F. Multi-Channel and Multi-Angle Algorithms for Estimating Sea and Land Surface Temperature with ATSR Data. *Int. J. Remote Sens.* **1996**, *17*, 2089–2114. [CrossRef]
32. Wan, Z.; Dozier, J. A Generalized Split-Window Algorithm for Retrieving Land-Surface Temperature from Space. *IEEE Trans. Geosci. Remote Sens.* **1996**, *34*, 892–905. [CrossRef]
33. Qin, Z.; Dall'Olmo, G.; Karnieli, A.; Berliner, P. Derivation of Split Window Algorithm and Its Sensitivity Analysis for Retrieving Land Surface Temperature from NOAA-advanced Very High Resolution Radiometer Data. *J. Geophys. Res. Atmos.* **2001**, *106*, 22655–22670. [CrossRef]
34. Sun, D.; Pinker, R.T. Estimation of Land Surface Temperature from a Geostationary Operational Environmental Satellite (GOES-8). *J. Geophys. Res. Atmos.* **2003**, *108*, 4326. [CrossRef]
35. Jiménez-Muñoz, J.C.; Sobrino, J.A. A Generalized Single-channel Method for Retrieving Land Surface Temperature from Remote Sensing Data. *J. Geophys. Res. Atmos.* **2003**, *108*, 4688. [CrossRef]
36. Tang, B.; Bi, Y.; Li, Z.-L.; Xia, J. Generalized Split-Window Algorithm for Estimate of Land Surface Temperature from Chinese Geostationary FengYun Meteorological Satellite (FY-2C) Data. *Sensors* **2008**, *8*, 933–951. [CrossRef] [PubMed]
37. Rozenstein, O.; Qin, Z.; Derimian, Y.; Karnieli, A. Derivation of Land Surface Temperature for Landsat-8 TIRS Using a Split Window Algorithm. *Sensors* **2014**, *14*, 5768–5780. [CrossRef]
38. Li, Z.; Wu, H.; Duan, S.; Zhao, W.; Ren, H.; Liu, X.; Leng, P.; Tang, R.; Ye, X.; Zhu, J.; et al. Satellite Remote Sensing of Global Land Surface Temperature: Definition, Methods, Products, and Applications. *Rev. Geophys.* **2023**, *61*, 1–77. [CrossRef]
39. Reiners, P.; Sobrino, J.; Kuenzer, C. Satellite-Derived Land Surface Temperature Dynamics in the Context of Global Change—A Review. *Remote Sens.* **2023**, *15*, 1857. [CrossRef]
40. Price, J.C. Estimating Surface Temperatures from Satellite Thermal Infrared Data—A Simple Formulation for the Atmospheric Effect. *Remote Sens. Environ.* **1983**, *13*, 353–361. [CrossRef]
41. Qin, Z.; Karnieli, A.; Berliner, P. A Mono-Window Algorithm for Retrieving Land Surface Temperature from Landsat TM Data and Its Application to the Israel-Egypt Border Region. *Int. J. Remote Sens.* **2001**, *22*, 3719–3746. [CrossRef]
42. McMillin, L.M. Estimation of Sea Surface Temperatures from Two Infrared Window Measurements with Different Absorption. *J. Geophys. Res.* **1975**, *80*, 5113–5117. [CrossRef]
43. Becker, F.; Li, Z.-L. Towards a Local Split Window Method over Land Surfaces. *Int. J. Remote Sens.* **1990**, *11*, 369–393. [CrossRef]
44. Gillespie, A.; Rokugawa, S.; Matsunaga, T.; Cothern, J.S.; Hook, S.; Kahle, A.B. A Temperature and Emissivity Separation Algorithm for Advanced Spaceborne Thermal Emission and Reflection Radiometer (ASTER) Images. *IEEE Trans. Geosci. Remote Sens.* **1998**, *36*, 1113–1126. [CrossRef]
45. Tonooka, H. An Atmospheric Correction Algorithm for Thermal Infrared Multispectral Data over Land-a Water-Vapor Scaling Method. *IEEE Trans. Geosci. Remote Sens.* **2001**, *39*, 682–692. [CrossRef]
46. Wan, Z.; Li, Z.-L. A Physics-Based Algorithm for Retrieving Land-Surface Emissivity and Temperature from EOS/MODIS Data. *IEEE Trans. Geosci. Remote Sens.* **1997**, *35*, 980–996. [CrossRef]

47. Zhao, Z.-Q.; He, B.-J.; Li, L.-G.; Wang, H.-B.; Darko, A. Profile and Concentric Zonal Analysis of Relationships between Land Use/Land Cover and Land Surface Temperature: Case Study of Shenyang, China. *Energy Build.* **2017**, *155*, 282–295. [CrossRef]
48. He, B.-J.; Zhao, Z.-Q.; Shen, L.-D.; Wang, H.-B.; Li, L.-G. An Approach to Examining Performances of Cool/Hot Sources in Mitigating/Enhancing Land Surface Temperature under Different Temperature Backgrounds Based on Landsat 8 Image. *Sustain. Cities Soc.* **2019**, *44*, 416–427. [CrossRef]
49. Li, J.; Song, C.; Cao, L.; Zhu, F.; Meng, X.; Wu, J. Impacts of Landscape Structure on Surface Urban Heat Islands: A Case Study of Shanghai, China. *Remote Sens. Environ.* **2011**, *115*, 3249–3263. [CrossRef]
50. Chen, A.; Yao, L.; Sun, R.; Chen, L. How Many Metrics Are Required to Identify the Effects of the Landscape Pattern on Land Surface Temperature? *Ecol. Indic.* **2014**, *45*, 424–433. [CrossRef]
51. Saudi Arabia Population Statistics 2023. Available online: https://www.stats.gov.sa/en (accessed on 10 October 2024).
52. Elfadaly, A.; Shams eldein, A.; Lasaponara, R. Cultural Heritage Management Using Remote Sensing Data and GIS Techniques around the Archaeological Area of Ancient Jeddah in Jeddah City, Saudi Arabia. *Sustainability* **2019**, *12*, 240. [CrossRef]
53. Google Earth Engine Platform. Available online: https://earthengine.google.com/platform/ (accessed on 10 October 2024).
54. United States Geological Survey (USGS). Landsat 8 (L8) Data Users Handbook. Available online: https://www.usgs.gov/landsat-missions/landsat-8-data-users-handbook (accessed on 10 October 2024).
55. Bokaie, M.; Zarkesh, M.K.; Arasteh, P.D.; Hosseini, A. Assessment of Urban Heat Island Based on the Relationship between Land Surface Temperature and Land Use/Land Cover in Tehran. *Sustain. Cities Soc.* **2016**, *23*, 94–104. [CrossRef]
56. El-Hattab, M.; Amany, S.M.; Lamia, G.E. Monitoring and Assessment of Urban Heat Islands over the Southern Region of Cairo Governorate, Egypt. *Egypt. J. Remote Sens. Space Sci.* **2018**, *21*, 311–323. [CrossRef]
57. Shirani-bidabadi, N.; Nasrabadi, T.; Faryadi, S.; Larijani, A.; Shadman Roodposhti, M. Evaluating the Spatial Distribution and the Intensity of Urban Heat Island Using Remote Sensing, Case Study of Isfahan City in Iran. *Sustain. Cities Soc.* **2019**, *45*, 686–692. [CrossRef]
58. Dissanayake, D.; Morimoto, T.; Ranagalage, M.; Murayama, Y. Land-Use/Land-Cover Changes and Their Impact on Surface Urban Heat Islands: Case Study of Kandy City, Sri Lanka. *Climate* **2019**, *7*, 99. [CrossRef]
59. Simwanda, M.; Ranagalage, M.; Estoque, R.; Murayama, Y. Spatial Analysis of Surface Urban Heat Islands in Four Rapidly Growing African Cities. *Remote Sens.* **2019**, *11*, 1645. [CrossRef]
60. Sultana, S.; Satyanarayana, A.N.V. Assessment of Urbanisation and Urban Heat Island Intensities Using Landsat Imageries during 2000–2018 over a Sub-Tropical Indian City. *Sustain. Cities Soc.* **2020**, *52*, 101846. [CrossRef]

Disclaimer/Publisher's Note: The statements, opinions and data contained in all publications are solely those of the individual author(s) and contributor(s) and not of MDPI and/or the editor(s). MDPI and/or the editor(s) disclaim responsibility for any injury to people or property resulting from any ideas, methods, instructions or products referred to in the content.